Instabilities in the Coupled Equatorial Ocean-Atmosphere System

Henk A. Dijkstra and Paul C.F. Van der Vaart

Institute for Marine and Atmospheric research Utrecht – Utrecht University

Princetonplein 5, 3584 CC Utrecht, The Netherlands

1 Introduction

The large-scale interaction between the ocean and atmosphere is one of the important factors of natural climate variability. The El-Niño/Southern Oscillation (ENSO) phenomenon in the Tropical Pacific is one of the most prominent examples of climate variability on interannual time scales. ENSO has large effects on climate, even far outside the Pacific basin and occurs at relatively short time scales. Therefore, it is one of the best studied climate phenomena, both observational and theoretical. ENSO is now known as an oscillatory mode in the coupled ocean-atmosphere system, arising through large scale instabilities involving the sea surface temperature, the low level

atmospheric winds and movements of the ocean-atmosphere interface. After an introduction into the phenomenon and its basic physics, the remainder of the paper focusses on the nature of the instability causing the oscillation.

1.1 The El-Niño/Southern Oscillation phenomenon

The equatorial Tropical Pacific climate system is a complex dynamical system, involving strong coupling between the ocean and the atmosphere (Philander, 1990). The time-averaged sea surface temperature (SST hereafter) is characterized by a cold tongue (Fig. 1a) of 24 $^\circ$ C water in the Eastern Pacific and a warm pool of 30 $^\circ$ C near the western boundary of the basin. Once about every four year, the sea surface temperature (SST) in the Eastern Pacific increases by a few degrees over a period of about one year. These events are called El Niño (literally: the little boy), referring to the Christmas Child, since the maximum of the event is usually around December. The 1997/1998 El Niño had one of the largest amplitudes of this century. The SST anomaly pattern (with respect to the mean state in Fig. 1a) for December 1997 is plotted in Fig. 1b. El Niño is seen as a basin wide SST perturbation with a maximum amplitude near the South-American coast of about 3 $^\circ$ C.

One of the measures of the condition of the Eastern Pacific ocean is the NINO3 index, which gives the SST anomaly from the mean state averaged over the box $[150W - 90W] \times [5S - 5N]$; this index is therefore positive during an El Niño. The drawn curve in Fig. 2 shows the course of this index from $1950 - 1997$. El Niño episodes occur once every three to seven years and last more than one year, with substantial variations

in strength. The strongest El Niño's were those of 1982/1983 and 1997/1998 having about the same NINO3 amplitude.

Normally, the equatorial Pacific surface winds, the trade winds, are directed westward and are driven by a pressure difference between a high pressure region in the east (e.g., at Tahiti) and a low pressure region in the west (e.g., at Darwin). During an El Niño, the pressure is lower than normal in Tahiti and higher than normal in Darwin. These variations in atmospheric pressure are known as the Southern Oscillation. The Southern Oscillation index (SOI), the pressure difference between Tahiti and Darwin, is plotted as the dotted curve in Fig. 2. When this index is negative (positive), the westward surface winds are weak (strong).

Although the strong negative correlation between SOI and NINO3 in Fig. 2 is obvious, it took until 1969 (Bjerknes, 1969) before it was realized that the changes occurring in the atmosphere and the ocean are closely related. Warm water in the east causes a weakening of the trade winds, which in turn drives changes in the oceanic circulation which influence SST. The El Niño/Southern Oscillation is therefore a coupled ocean-atmosphere phenomenon. The warm phase of the oscillation coincides with El Niño (positive NINO3) in the ocean and with weak trade winds (negative SOI) in the atmosphere. The cold phase (also called La Niña: the little girl) coincides with strong trade winds (positive SOI) and lower than normal SST's (negative NINO3) in the eastern part of the equatorial Pacific.

1.2 Basic Physics

Over the years, measurements and modelling have lead to a better understanding of ENSO, based on the basic knowledge of the behavior of the ocean and the atmosphere. Under normal conditions, the trade winds induce a slope in the sea level along the equator (Fig. 3). In the west, the sea level is on average about 25 cm higher than in the east. Because of the higher hydrostatic pressure, the 20° C isotherm is pushed more downward in the west than in the east. The depth of this isotherm is a measure of the boundary between the warm surface water and the cold water below and is called the thermocline. The cold water is normally situated about 50 m from the surface in the east but is at much larger depth (at about 200 m) in the west (Fig. 3).

Frictional processes in the surface layer of the ocean and the Coriolis effect at slightly off-equatorial latitudes induce a northward (southward) (Ekman-) mass transport just north (south) of the equator. At the equator, this divergence is compensated by an upward flow bringing relatively cold water to the surface. Together, the slope in the thermocline and the upwelling cause the cold tongue of water in the east and the warm pool in the west. Air warms up above warm water and then rises which leads to convection and cloud formation while air descends over the cold water. Hence, the east-west SST contrast induces surface winds that blow from east to west, thus reinforcing the trade winds. The circulation driven by this zonal SST-gradient is called the Walker circulation.

A classical explanation of El Niño is that of a delayed oscillator (Suarez and Schopf, 1988). At the beginning of an El Niño the surface winds weaken which causes a change

in the slope of the sea level and the thermocline. The thermocline tends to flatten and, together with a reduced upwelling, this leads to a warming of the Eastern Pacific. This in turn causes a weakening of the Walker circulation, leading to a further weakening of the surface winds (Fig. 4). The ocean, however, does not immediately adapt to the changes in windstress. Long (Kelvin and Rossby) waves in the thermocline are excited to adapt to the changing forcing conditions at the surface. In the equatorial ocean, a Kelvin wave takes about two months to travel from west to east, and a Rossby wave about six months to travel in the opposite direction. During an El Niño, the easterly thermocline lies deeper on the equator, but less deep in areas just to the north and the south of the equator. These off-equatorial shallower areas first propagate to the west, reflect at the west coast of the Pacific, and then travel to the east. Arriving at their easterly destination, they cause a shallowing of the thermocline which terminates El Niño.

In more modern terms, ENSO is viewed as an oscillatory mode in the coupled ocean-atmosphere system. During this oscillation, the surface winds strengthen and weaken due to variations in SST, which induces changes in the ocean circulation. The latter affect SST and the phase differences needed for the oscillation are due to the adaption processes of the ocean, involving a basin wide reorganization of the thermocline.

2 The Zebiak-Cane model

One of the first models that is able to reasonably simulate ENSO is that of Zebiak and Cane (1987). In its original version, an annual mean state and seasonal cycle of both

ocean and atmosphere is obtained from observations and the evolution of anomalies with respect to this reference state are computed. The model produces recurring warm events that are irregular in both amplitude and spacing, but favor a 3-4 year period.

The model describes large scale motions in the tropical ocean and atmosphere in a domain of infinite extent in the latitudinal direction (y). The ocean is bounded by meridional walls representing the coasts of Asia ($x = 0$) and America ($x = L$). The ocean component of the model consists of a well-mixed layer of mean depth H_1 embedded in a shallow water layer of mean depth $H = H_1 + H_2$ having a constant density ρ_1 (Fig. 5). Only long wave motions above the thermocline are considered and the deep ocean (having a constant density ρ_2) is assumed to be at rest. Deviations from the averaged thermocline depth H are indicated by h and the horizontal velocities u and v are the dynamical variables in this layer. The evolution of both velocity and thermocline anomalies are governed by the shallow water equations on an equatorial β-plane driven by a windstress $\tau = (\tau^x, \tau^y)$. The equations are (Philander, 1990)

$$\frac{\partial u}{\partial t} + \epsilon_o u - \beta y v + g' \frac{\partial h}{\partial x} = \frac{\tau^x}{\rho_1 H} \tag{1a}$$

$$\beta y u + g' \frac{\partial h}{\partial y} = \frac{\tau^y}{\rho_1 H} \tag{1b}$$

$$\frac{\partial h}{\partial t} + \epsilon_o h + H\left(\frac{\partial u}{\partial x} + \frac{\partial v}{\partial y}\right) = 0 \tag{1c}$$

where $g' = g(\rho_2 - \rho_1)/\rho_1$ is the reduced gravity and ϵ_o is a friction coefficient. The characteristic velocity in the ocean is given by $c_0 = (g'H)^{\frac{1}{2}}$, which is the phase speed of the first free baroclinic Kelvin wave. The boundary conditions are

$$\int_{-\infty}^{\infty} u(0,y,t)dy = 0 \ , \ u(L,y,t) = 0 \tag{2}$$

The first condition models that the net mass flux through the western boundary ($x = 0$) is zero, while the second is a kinematic condition on the eastern boundary ($x = L$) corresponding to zero normal flow.

The intensification of wind-driven currents through rotation and frictional processes is modelled through a fixed depth Ekman surface layer. The zonal and meridional velocities in this layer are u_s and v_s respectively and the governing equations are given by (Zebiak and Cane, 1987)

$$\epsilon_s u_s - \beta y v_s = \frac{H_2}{H_1}\frac{\tau^x}{\rho_1 H} \tag{3a}$$

$$\epsilon_s v_s + \beta y u_s = \frac{H_2}{H_1}\frac{\tau^y}{\rho_1 H} \tag{3b}$$

in which ϵ_s models the surface layer friction.

The horizontal velocities (u_1, v_1) influencing the heat transport in the mixed layer consist of two components, i.e.

$$u_1 = u + u_s \ ; \ v_1 = v + v_s \tag{4}$$

The velocities without subscripts are due to the vertical mean currents above the thermocline and the other part is due to the vertical shear currents associated with the fixed depth surface layer. The vertical velocity component, the upwelling, is determined from continuity

$$w_1 = H_1(\frac{\partial u_1}{\partial x} + \frac{\partial v_1}{\partial y}) \tag{5}$$

The evolution of the mixed layer temperature T is governed by the equation

$$\frac{\partial T}{\partial t} + \epsilon_w(T - T_0) + \frac{w_1}{H_1}\mathcal{H}(w_1)(T - T_{sub}(h)) + u_1\partial_x T + v_1\partial_y T = 0 \tag{6}$$

where $\mathcal{H}$ is a continuous approximation of the Heaviside function. The second term in (6) is the Newtonian cooling term, with inverse damping time ϵ_w, representing all vertical processes as mixing, sensible and latent heat fluxes, and long wave and shortwave radiation. T_0 is the temperature of radiative equilibrium which is realized in the absence of large-scale horizontal motion in the upper ocean and atmosphere. The next term models the heat flux due to upwelling through the total velocity w_1 and the approximate vertical temperature gradient $(T - T_{sub}(h))/H_1$. The subsurface temperature (T_{sub}) depends on the thermocline deviations and models the effect that heat is transported upwards (if $w_1 > 0$) when the cold water is further from the surface. It is parameterized by

$$T_{sub}(h) = T_{s0} + (T_0 - T_{s0})tanh(\frac{h + h_o}{H}), \tag{7}$$

where h_o is some offset value. In this formulation, T_{sub} cannot exceed T_0 and cannot decrease below $2T_{so} - T_0$). The last two terms in (6) represent horizontal advection.

The atmospheric zonal and meridional boundary-layer velocities (u_a, v_a) and geopotential Φ (proportional to sea level pressure) are assumed to adapt instantaneously to the forcing. The atmospheric circulation is forced by sea surface temperature anomalies

with respect to T_0. The dynamics of the atmosphere component follow Gill (1980) with the mechanical balances being between Coriolis force, pressure gradient and boundary layer friction, while the thermodynamical balances are between diabatic heating and divergent flow. The equations are

$$\epsilon_a u_a - \beta y v_a + \frac{\partial \Phi}{\partial x} = 0 \tag{8a}$$

$$\beta y u_a + \frac{\partial \Phi}{\partial y} = 0 \tag{8b}$$

$$\epsilon_a \Phi + c_a^2 (\frac{\partial u_a}{\partial x} + \frac{\partial v_a}{\partial y}) = -\alpha_T (T - T_0) \tag{8c}$$

where ϵ_a represents boundary layer friction and α_T is a proportionality constant relating SST anomalies and heat forcing. The constant c_a is the phase speed of the first baroclinic Kelvin wave in the atmosphere Gill (1980).

The model equations are closed by prescribing how the windstress τ is determined from the atmosphere model. Following Dijkstra and Neelin (1995), we assume that the windstress is only zonal ($\tau^y = 0$) and part of the windstress, say τ_{ext}, is unrelated to coupled processes within the basin. Even in the absence of zonal SST gradients, there still would be a weak zonal circulation, for example, driven by the zonally asymmetric land-sea contrast. The remainder is induced by the basin wide zonal SST-gradient and is assumed proportional the zonal surface velocity. Hence,

$$\tau^x = \tau_{ext} + \gamma u_a \tag{9}$$

In the coupled model, the winds can be calculated once the SST deviations from T_0 are known. From the winds, the ocean response in both shallow water and surface

layer is determined and subsequently the SST can be calculated from (6). The numerical details for solving the set of governing equations can be found in Van der Vaart *et al.* (1998). Variables are expanded into spectral basis functions, with Chebychev polynomials in zonal direction and Hermite functions in meridional direction. Using collocation techniques, a set of nonlinear algebraic equations is obtained for the steady states of the model. The analysis of the stability of these steady states leads to a generalized eigenvalue problem. Both steady states and their linear stability are traced through parameter space using continuation techniques (Dijkstra *et al.*, 1995).

3 Bifurcation analysis of the Zebiak-Cane model

The Zebiak-Cane model turn out to be very well suited to determine the details of the evolution of ENSO events and has been widely used to study their physics. Many results of this model have been reviewed in Neelin *et al.* (1994), where also many references can be found. From these results, it appears that a large scale instability of the coupled ocean-atmosphere plays a major role in the dynamics of ENSO. It is this instability, which is the focus of the results below.

3.1 The warm pool/cold tongue mean state

The control parameter in the system is the coupling parameter μ, which is a dimensionless product of α_T and γ. Its physical interpretation is the amount of windstress per degree SST anomaly. Other parameters are fixed at their 'best' values as estimated from observations. At zero coupling ($\mu = 0$), the ocean circulation and consequently

SST is determined by the external zonal windstress τ_{ext}. This windstress is assumed to have the form

$$\tau_{ext} = -F_0 \; e^{-\frac{(\alpha y)^2}{2}} \tag{10}$$

where α controls the meridional extension of the external wind. The amplitude F_0 corresponds to a dimensional value of 0.01 Pa which is about 10% of the observed windstress. At each latitude, the external wind is zonally constant. In response to the external wind, the equatorial temperature, say T_{ext}, increases monotonically from about 25.5 $^\circ C$ in the east to about 28.5 $^\circ C$ in the west. The thermocline is approximately linear at the equator, its depth is increasing westwards and it has slight off-equatorial maxima near the western boundary.

At small μ, the additional windstress due to coupling is approximately the atmospheric response to the cooling $T_{ext} - T_0$. This enhances the westward winds over most of the basin, leading to larger upwelling and a stronger thermocline slope, strengthening the cold tongue in the eastern part of the basin. The temperature $(T - T_0)_{EC}$ of the cold tongue and the vertical velocity just below the cold tongue w_E (Fig. 6) demonstrate that there is a unique steady solution as a function of μ, with more upwelling as coupling gets stronger.

At $\mu = 0.5$, the spatial structure of the mean state is shown in Fig. 7. The zonal scale of the cold tongue (panel a) is set by a delicate balance of thermocline and surface layer feedbacks (Dijkstra and Neelin, 1995). The meridional extent of the cold tongue is determined both by the Ekman spreading length (ϵ_s/β) and by meridional

advection. The thermocline field (panel b) displays the off-equatorial maxima and a deeper (shallower) equatorial thermocline in the west (east). This indicates that the reservoir of heat content lies off-equatorial in the central and western part of the basin. The zonal wind response u_a (panel c) shows the intensification of the westward winds, with a maximum west of the cold tongue. The vertical velocity structure (panel d) is clearly controlled by Ekman divergences. Upward velocities are restricted to an equatorial zone and the maximum amplitude occurs in the eastern part of the basin.

3.2 Linear stability of the coupled climatology

Along the branch of steady states in Fig. 6 the linear stability is determined simultaneously, by writing the total solution vector ϕ, consisting of ocean, atmosphere quantities and SST, as

$$\phi(x, y, t) = \overline{\phi}(x, y) + \tilde{\phi}(x, y)\ e^{\sigma t}. \tag{11}$$

Here, the vector $\overline{\phi}$ represents the mean state, $\tilde{\phi}$ perturbations with respect to this mean state and σ is the complex growth rate of the perturbation. In Fig. 8, the path of six modes – which become leading eigenmodes at high coupling – is plotted as a function of the coupling strength μ. In panel (a), a larger dot size indicates a larger value of μ and both period and growth rate of the modes are given in year^{-1}. In panel (b) only the growth rate is plotted against μ. One oscillatory mode becomes unstable as μ is increased and a Hopf bifurcation occurs near $\mu = 0.5$.

At the critical value $\mu_c = 0.5$, for which the mean state was shown in Fig. 7,

time-longitude diagrams of the equatorial thermocline, temperature and zonal wind anomalies of this oscillatory mode are shown in Fig. 9. The SST pattern (panel b) displays a nearly standing oscillation for which the spatial scale is confined to the cold tongue of the mean state. There is a slight eastward propagation of the SST anomaly in the central equatorial Pacific. The thermocline anomaly (panel a) shows western anomalies in heat content leading those with the same sign at the eastern boundary. These anomalies are out of phase with the SST anomalies with a lag of about 5 months. The wind response (panel c) is much broader zonally and is in phase with the SST anomaly. Although the wind maximum in the central Pacific is more to the east than in observations, the time-longitude diagrams do correspond reasonably to those observed (Neelin *et al.*, 1994).

The phase relationships between wind/SST-anomalies and thermocline anomalies can be seen more clearly in Fig. 10. Here, the thermocline depth in the western Pacific h_W and the zonal mean equatorial thermocline displacement h_{ZM} are related to the SST anomaly in the eastern Pacific (at $x/L = 0.92$) over one cycle of the oscillation. Panel (a) shows the characteristic ENSO phase relationship between SST and thermocline anomalies with a relatively shallow (deep) western thermocline in case of a warm (cold) event. As the closed curve is traversed clockwise over one cycle of the oscillation, it is seen that a cold event is followed by an extreme positive western thermocline anomaly. As the SST anomaly becomes zero, the western thermocline anomaly is still positive and panel (b) shows that this also holds for the zonally averaged thermocline anomaly. Hence, the equatorial heat content is slowly built up after the cold event

by the increase of the trade winds. This sets the stage for the following warm event in which the equatorial heat content is discharged. After the warm event, the zonally averaged thermocline anomaly is negative as the SST anomaly goes through zero again and the equatorial heat content is low, which causes the next cold event.

The meridional structure of the ENSO mode is shown by plotting the different fields (Figs. 11 to 13) at several phases of the oscillation relative to the period, i.e. phase $t = 1/2$ indicates the fields after half a period. The starting point of the description is a positive SST-anomaly in the eastern Pacific (early El-Niño phase), as shown in Fig. 11 at $t = 0$. Eastward zonal wind anomalies to the west of the maximum in SST-anomaly (Fig. 11) are present as can be seen in Fig. 13 at $t = 0$. The wind response amplifies the positive SST-anomaly ($t = 1/16$ to $1/8$) and the spatial scale of the SST anomaly is controlled by the shape of the cold tongue (cf. Fig. 7). The equatorial thermocline response to the weaker surface winds up to $t = 1/8$ results in a negative anomaly (i.e. negative heat content) in the Western Pacific (Fig. 12, $t = 1/8$). This anomaly is at its minimum a few months later than the maximum of equatorial SST. As long as the positive thermocline/SST-anomaly in the eastern part of the basin does not weaken, this negative anomaly cannot be discharged. However, due to ocean wave reflections at the eastern boundary, the mass fed along the equator to the eastern basin is transformed into a collective of long Rossby waves which propagates westward (Fig. 12, $t = 0 - 1/8$).

At the equator, the eastern positive thermocline anomaly and consequently the SST anomalies are weakened. This reduces the east-west SST gradient, causing the

anomalous eastward winds to weaken (Fig. 13, t = 1/8 to 5/16). Termination of the El Niño phase sets in, as the western warm pool discharges its previously built up negative heat content (t = 3/8 through 7/16 in Fig. 12). This is characteristic of the recharge oscillator (Jin, 1997a), showing a negative zonally mean thermocline anomaly at the equator during the transition from warm to cold SST anomalies. As the thermocline rises in the east, the SST anomaly becomes negative and through coupled processes its amplitude increases. The trade winds recover (Fig. 13, t = 7/16) and the positive off-equatorial thermocline anomalies propagate westwards (Fig. 12, t = 3/8 - 7/16). Then the cycle starts over again but with the signs of the perturbations reversed.

3.3 Weakly nonlinear analysis

The results of the linear stability analysis do not provide information on the finite amplitude of the fields for supercritical conditions. In this section, the equilibration of the perturbations to finite amplitude is studied in a weakly nonlinear context, i.e. for coupling values of μ just above the Hopf-bifurcation. Let

$$\epsilon = \frac{\mu - \mu_c}{\mu_c} \ll 1 \ , \tag{12}$$

be a measure of the distance beyond critical conditions, i.e. $\mu = \mu_c$ at which $Re(\sigma) = 0$. For these values of the coupling strength μ, equilibration of the unstable perturbations will occur on a time-scale long compared to the time-scale of growth. Therefore a new time-variable is introduced

$$\tau = \epsilon^2 t \tag{13}$$

Coupling strength μ, time and the solution vector ϕ are expanded in terms of ϵ and the fundamental mode with time-dependence $e^{i\omega_c t}$, where $\omega_c = Im(\sigma)$ at $\mu = \mu_c$,

$$\phi = \overline{\phi} + \epsilon A(\tau)\tilde{\phi}e^{i\omega_c t} \quad + \quad \epsilon^2(|A(\tau)|^2\tilde{\phi}_{02} + A^2(\tau)\tilde{\phi}_{22}e^{2i\omega_c t}) + \epsilon^3\tilde{\phi}_{13}e^{i\omega_c t} + c.c. \tag{14a}$$

$$\partial_t \quad \rightarrow \quad i\omega_c + \epsilon^2\partial_\tau \tag{14b}$$

$$\mu \quad = \quad \mu_c(1 + \epsilon^2 m)\ , \qquad m = \mathcal{O}(1) \tag{14c}$$

In these expansions, *c.c.* denote complex conjugate, m is the new control parameter, and $A(\tau)$ is the (complex) amplitude of the initially unstable mode with spatial structure $\tilde{\phi}$.

By substitution of the expansions (14) into the governing equations and collecting terms of like orders in ϵ and $e^{i\omega_c t}$, one can reduce the full equations to a scalar equation for the amplitude $A(\tau)$. This becomes a Landau equation

$$\frac{\partial A}{\partial \tau} = m\frac{\partial \sigma}{\partial \mu}A - \Lambda A|A|^2 \tag{15}$$

where the coefficients are evaluated at $\mu = \mu_c$ and which are calculated numerically within the spectral set-up (Van der Vaart and Dijkstra, 1997). Solving (15) for A, the solution for the SST field becomes

$$T(x, y, t) = \overline{T}(x, y) + \epsilon A(\tau)\tilde{T}(x, y)e^{i\omega_c t} + \mathcal{O}(\epsilon^2) \tag{16}$$

where the mean state is represented by $\overline{T}$ and the critical mode by $\tilde{T}$. If the coefficients $\frac{\partial\sigma}{\partial\mu}$ and Λ satisfy the conditions for a supercritical Hopf bifurcation, $Re(\sigma_\mu) > 0$ and $Re(\Lambda) > 0$, finite amplitude solutions to (15) exist of the form

$$A(\tau) = ge^{i\Omega\tau} \; ; \; g = \sqrt{\frac{Re(\frac{\partial\sigma}{\partial\mu})}{Re(\Lambda)}} \; ; \; \Omega = Im(\frac{\partial\sigma}{\partial\mu}) - \frac{Im(\Lambda)}{Re(\Lambda)} \tag{17}$$

Using these expressions one can derive the amplitude and total period of the stable limit cycle for coupling values beyond the Hopf-bifurcation. For example, the period P is given by

$$P = \frac{2\pi}{\omega_c + \epsilon^2\Omega}, \tag{18}$$

In Fig. 14a the period of the periodic orbit is plotted as a function of the coupling strength μ. The period of ENSO oscillation is set by the critical period (at the Hopf-bifurcation), rather than the frequency of the instability at supercritical coupling strength which is also found in other studies (Battisti and Hirst, 1989; Neelin *et al.*, 1994; Jin, 1997b). The amplitude of the SST-anomaly in the cold tongue increases strongly with coupling being about 3 $^\circ C$ for $\epsilon = 0.1$.

3.4 Irregular behavior of ENSO

Temporal variability in the Tropical Pacific does not only occur on interannual time scales. One other major time-dependent phenomenon in the Tropical Pacific is the seasonal cycle (Horel, 1982). At the equator, SST are warmest during winter-spring and are coldest during summer-fall when the northward winds are maximal. The

annual component of the seasonal cycle in the Eastern Pacific is a strange phenomenon considering the semi-annual component of the forcing. It is by now clear that coupled processes, in particular those in the surface layer, are involved to get an annual response to a semi-annual forcing (Chang *et al.*, 1995). The interaction of seasonal cycle and ENSO variability can lead to very complicated temporal behavior (Jin *et al.*, 1994; Tziperman *et al.*, 1994; Chang *et al.*, 1996). It was shown that the interactions of an externally forced seasonal cycle and the internal ENSO oscillation lead to subharmonic frequency locking and chaotic behavior.

Transient simulations using variants of the Zebiak-Cane model in the strongly nonlinear regime and subjected to seasonal forcing with annual period and atmospheric (white) noise (Jin *et al.*, 1996; Tziperman *et al.*, 1995) lead to the understanding that the seasonal cycle controls the timing of warming events whereas the noise forcing is the most likely candidate for ENSO irregularity. An example of results of such a simulation using the model above at supercritical conditions ($\mu = 0.7$) is shown in the time-longitude diagrams of Fig. 15. The deterministic period of the supercritical solution retains its identity over the influence of the seasonal and stochastic forcing (Fig. 16a). The phase space view of Eastern Pacific SST anomaly versus Western Pacific thermocline depth anomaly (Fig. 16b) shows the effect of the noise as a fuzzy signature of the otherwise stable periodic orbit. This broadening compares with results using more complicated models Blanke *et al.* (1997).

4 Summary

A bifurcation analysis of an intermediate complexity model has been performed to study the physics of the El Niño/Southern Oscillation phenomenon. Both the mean state and the instabilities are determined by coupled processes between the ocean and atmosphere. An external wind induces a weak zonal SST gradient, with non-zero upwelling and a small thermocline slope. The SST gradient is amplified by the coupled processes to give the cold tongue/warm pool spatial structure of the mean state. The amplitude of the cold tongue depends on the coupling strength μ.

This state becomes unstable to a single oscillatory mode as the coupling strength is increased. The mechanism of this mode is a large scale instability, involving motion at the air-sea interface and in the thermocline, and the strengthening/weakening of the trade winds due to anomalies in SST. The ocean provides the memory of the oscillation because it does not only respond to actual winds, but also to past winds due to the propagation of waves in the thermocline. The spatial pattern of the mean state is important to set the location where amplification of disturbances can occur. As the cold tongue warms, the tradewinds relax, the equatorial thermocline tilt reduces, and the deepening of the east Pacific thermocline further amplifies the SST warming within the cold tongue. Due to ocean wave reflections at the eastern boundary, mass is exchanged from the equatorial region towards off-equatorial latitudes. This causes the discharge of equatorial heat content which weakens the SST anomaly and thereby the wind anomaly. When the SST and wind anomalies diminish, this discharge process of equatorial ocean heat content continues, leading to an anomalously shallow thermocline over the entire

equator. Upwelling is able to induce negative SST anomalies and therefore induces the cold phase of ENSO. This recharge oscillation mechanism, first envisioned by Wyrtki (1985) and Cane and Zebiak (1985), and later illustrated by Jin (1996, 1997a), is clearly consistent with the ENSO mode found here as the critical mode of the coupled model.

A weakly nonlinear analysis shows that the spatial pattern of the periodic orbit and its period are quite insensitive to the coupling strength. As soon as supercricital conditions are reached, hardly any change in period occurs, although the magnitude of the actual perturbation amplitude increases with μ. When the system is forced with a seasonal signal and white noise, the spectral peak of the ENSO mode broadens. When the oscillatory mode is not unstable, i.e. μ is below the critical value for instability, the mode still may be excited by stochastic forcing from the atmosphere (Blanke *et al.*, 1997). The degree of sub- or supercriticality, which is hard to establish from observations, is essential whether irregularity of the ENSO cycle can be attributed to deterministic processes, i.e. interaction with the seasonal cycle or whether stochastic noise processes are essential.

Models like the Zebiak-Cane model have trouble to simulate a correct seasonal cycle as obtained from semi-annual forcing. On the path to a unified theory for the mean state, the seasonal cycle and the interannual variability in the Tropical Pacific, next step in the analysis is to study the stability of such a seasonal cycle along similar lines as in Jin *et al.* (1996). The Zebiak-Cane model has to be modified since its off-equatorial response is not adequate to simulate the equatorial asymmetry of the seasonal cycle. Furthermore, the tropical climate system has to be studied within the global climate

system to account for the influence of tropical-extratropical interactions. The behavior of ENSO is anything but regular when viewed on a longer time scale. Burning questions are whether the intensity of El Niño varies over decades. A knowledge of this natural variability is necessary in order to determine whether changes in ENSO behaviour can be expected as a result of the increase of greenhouse gases in the atmosphere.

Much has been learned over the last decades. The 1982/1983 El Niño was a total surprise to all and only with hindsight it could be seen that something unusual had happened (Philander, 1990). During the last El Niño, the situation has been totally different, with measurements of the state of the Tropical Pacific being distributed world wide via the Internet and various centres providing operational El Niño forecasts and advice. Models have shown very different prediction skills and have indicated that details in the dynamics can make a difference between succesful prediction or a failure. The theoretical research using intermediate complexity models such as the Zebiak-Cane model has been and is still very useful to understand the physics of the results of more elaborate models and for suggesting improvements of these models.

Acknowledgments This work was supported by the Dutch National Research Programme on Global Air Pollution and Climate Change (N.R.P.) within project 951235. All computations were performed on the CRAY C916 at the Academic Computing Centre (SARA), Amsterdam, the Netherlands within project SC283 and SC498. Use of these computing facilities was sponsored by the National Computing Facilities Foun-

dation (N.C.F.) with financial support from the Netherlands Organization for Scientific Research (N.W.O.). Collaboration with David Neelin (UCLA, Los Angeles, USA) and Fei Fei Jin (UH, Honolulu, USA) over the years is much appreciated.

References

Battisti, D. and Hirst, A. (1989). Interannual variability in a tropical atmosphere-ocean model: Influence of the basic state, ocean geometry and nonlinearity. *J. Atm. Sc.*, **46**, 1687–1712.

Bjerknes, J. (1969). Atmospheric teleconnections from the equatorial Pacific. *Mon. Wea. Review*, **97**, 163–172.

Blanke, B., Neelin, J. D., and Gutzler, D. (1997). Estimating the effect of stochastic wind stress forcing on ENSO irregularity. *J. Clim.*, **10**, 1473–1486.

Cane, M. and Zebiak, S. (1985). A theory for El Niño and the Southern Oscillation. *Science*, **228**, 1084–1087.

Chang, P., Ji, L., Wang, B., and Li, T. (1995). Interactions between the seasonal cycle and El Niño-Southern Oscillation in an intermediate coupled ocean-atmosphere model. . *J. Atm. Sc.*, **52**, 2353 – 2372.

Chang, P., Ji, L., Li, H., and Flügel, M. (1996). Chaotic systems versus stochastic processes in El Niño-Southern Oscillation in coupled ocean-atmosphere models. *Physica D*, **98**, 301–320.

Dijkstra, H. and Neelin, J. D. (1995). Coupled ocean-atmosphere interaction and the tropical climatology, part II: Why the cold tongue is in the east. *J. Clim.*, **8**, 1343–1359.

Dijkstra, H., Molemaker, M., van der Ploeg, A., and Botta, E. (1995). An efficient code to compute nonparallel flows and their linear stability . *Comp. Fluids*, **24**, 415–434.

Gill, A. (1980). Some simple solutions for heat induced tropical circulation. *Quart. J. Roy. Meteor. Soc.*, **106**, 447–462.

Horel, J. (1982). The annual cycle in the Tropical Pacific atmosphere and ocean. *Monthly Weather Review*, **110**, 1863–1878.

Jin, F.-F. (1996). Tropical ocean-atmosphere interaction, the Pacific Cold Tongue, and the El Niño/Southern Oscillation. *Science*, **274**, 76–78.

Jin, F.-F. (1997a). An equatorial recharge paradigm for ENSO: Part I: Conceptual Model. *J. Atm. Sc.*, **54**, 811–829.

Jin, F.-F. (1997b). An equatorial recharge paradigm for ENSO: Part II: A stripped-down coupled model. *J. Atm. Sc.*, **54**, 830–8847.

Jin, F.-F., Neelin, J. D., and Ghil, M. (1994). El Niño on the devil's staircase: Annual subharmonic steps to chaos. *Science*, **264**, 70–72.

Jin, F.-F., Neelin, J. D., and Ghil, M. (1996). El Niño/Southern Oscillation and the annual cycle: Subharmonic frequency-locking and aperiodicity. *Physica D*, **98**, 442–465.

Neelin, J. D., Latif, M., and Jin, F. (1994). Dynamics of coupled ocean-atmosphere models: The tropical problem. *Ann. Rev. Fluid Mech.*, **26**, 617–659.

Philander, S. (1990). *El-Niño and the Southern Oscillation.* Academic Press, New York.

Suarez, M. and Schopf, P. S. (1988). A delayed action oscillator for ENSO. *J. Atm. Sc.*, **45**, 3283–3287.

Tziperman, E., Stone, L., Cane, M., and Jarosh, H. (1994). El Niño chaos: overlapping of resonances between the seasonal cycle and the Pacific ocean-atmosphere oscillator. *Science*, **264**, 72–74.

Tziperman, E., Cane, M., and Zebiak, S. (1995). Irregularity and locking to the seasonal cycle in an ENSO prediction model as explained by the quasi-periodicity route to chaos. *J. Atm. Sc.*, **52**, 293–306.

Van der Vaart, P. and Dijkstra, H. (1997). Sideband instabilities of mixed barotropic/ baroclinic waves growing on a midlatitude zonal jet. *Phys. Fluids*, **9**, 615–631.

Van der Vaart, P. C., Dijkstra, H., and Jin, F.-F. (1998). The Pacific Cold Tongue and the ENSO mode . *J. Atm. Sc., submitted*.

Wyrtki, K. (1985). Water displacements in the Pacific and the genesis of El Niño cycles. *J. Geoph. Res.*, **91**, 7129–7132.

Zebiak, S. and Cane, M. (1987). A model El Niño-Southern Oscillation. *Monthly Weather Review*, **115**, 2262–2278.

Captions to the Figures

Figure 1.

(a) Annual mean sea surface temperature in the Tropical Pacific. Along the equator, contour levels are in degrees C. (b) SST anomaly pattern for December 1997. Light areas indicate zero anomalies, whereas darker shading indicates positive anomalies, with a maximum amplitude of $3\ ^\circ C$.

Figure 2.

Time series of the SST anomaly averaged over a box in the Eastern Pacific (NINO3) and the difference in sea level pressure (SOI) between Tahiti (Eastern Pacific) and Darwin (Western Pacific) .

Figure 3.

Sketch of normal ocean-atmosphere conditions. The slope in the boundary between warm surface water and the colder water below (the thermocline) is idealized as being constant. Westward surface winds induce a slope in sea level and thermocline and casue, togetherwith equatorial upwelling, the characteristic cold tongue/warm pool SST structure.

Figure 4.

Ocean-atmosphere conditions during an El Niño event with a flattened sea level and thermocline, a weak Walker Circulation and a reduced upwelling causing the relatively

warm SST in the Eastern Pacific.

Figure 5.

Schematic representation of the Zebiak-Cane model showing both surface layer and shallow water layer, the latter bounded below by the thermocline.

Figure 6.

Eastern Pacific ($x/L = 0.8$) equatorial SST deviation from $T_0 = 30\ ^\circ C$ (a) and upwelling velocity (b) as a function of the coupling strength μ.

Figure 7.

The mean state at standard parameter values and $\mu = 0.5$ in the $X = x/L$ and $Y = y/\lambda$ plane, where $\lambda = (c_0/\beta)^{\frac{1}{2}}$ is a characteristic meridional lengthscale. (a) $T - T_0$; maximum 6.6 $^\circ C$. (b) Thermocline depth; maximum 82.3 m. (c) Zonal wind u_a; maximum 9.5 m/s. (d) Vertical velocity w_1; maximum 1.44 m/day. In all panels, values are scaled with the maximum value of each field and the contour levels (with interval 0.069) are with respect to this maximum.

Figure 8.

(a) Plot of the eigenvalues for the six leading eigenmodes in the $(Re(\sigma), Im(\sigma))$-plane. Values of the coupling strength μ are represented by dot size (smallest dot is the uncoupled case ($\mu = 0$) for each mode, largest dot is the fully coupled case at the

Hopf bifurcation ($\mu_c = 0.5$)). The Hopf-bifurcation that yields the ENSO mode occurs where the path of one eigenvalue first crosses $Re(\sigma) = 0$. (b) The growth rate of the leading modes as a function of coupling strength.

Figure 9.

Time (t)-longitude (X=x/L) diagram at the equator of the anomalies of (a) SST (max = 1.4 $°C$), (b) thermocline depth (max. = 9.5 m), and (c) zonal wind (max. = $3.0m/s$). The period of the oscillation is 3.7 years. Note that the amplitude of the oscillation is not determined by the linear stability analysis. The maximum amplitudes are relative magnitudes of the different fields, i.e. the mode displays a thermocline deviation of about 10 m per degree SST anomaly.

Figure 10.

(a) Phase relation between the equatorial thermocline depth anomaly in the western part of the basin and the SST anomaly in the east. (b) The phase relation between the zonally averaged equatorial thermocline anomaly h_{ZM} and SST anomaly in the east (T_E). Note that the amplitudes in both panels are arbitrary, but that their ratio is fixed. The direction of rotation is clockwise in both cases.

Figure 11.

Planforms of the SST anomaly during the oscillation in the X-Y plane; times are with respect to the period of the oscillation. Drawn (dotted) lines represent warm (cold)

anomalies.

Figure 12.

Planforms of the thermocline anomaly during the oscillation as in Fig. 11. Drawn (dotted) lines represent positive (negative) anomalies.

Figure 13.

Planforms of the zonal wind anomaly during the oscillation as in Fig. 11. Drawn (dotted) lines represent anomalous eastward (westward) winds.

Figure 14.

The frequency (a) and amplitude (b) of the finite amplitude limit cycle as obtained from the weakly nonlinear analysis within the fully coupled Zebiak-Cane model in a finite ocean basin. Shown is the maximum amplitude of the SST anomaly near the position of the cold tongue.

Figure 15.

Equatorial time-longitude diagrams of anomalies of (a) $(T - T_0)$ (maximum = $5.732\ ^\circ C$) , (b) thermocline depth (maximum = $71\ m$) and (c) zonal wind (maximum = $16.5\ m\ s^{-1}$). Simulation at supercritical conditions, with stochastic forcing and seasonal cycle included. Dark (light) colors represent negative (positive) anomalies.

Figure 16.

(a) Powerspectrum of equatorial SST at ($x/L = 0.8$), for the case of supercritical coupling strength (with respect to the annual mean state) with stochastic forcing and seasonal cycle included.(b) Phase space view of eastern Pacific SST anomaly (T_E) versus western Pacific thermocline depth anomaly (h_W).

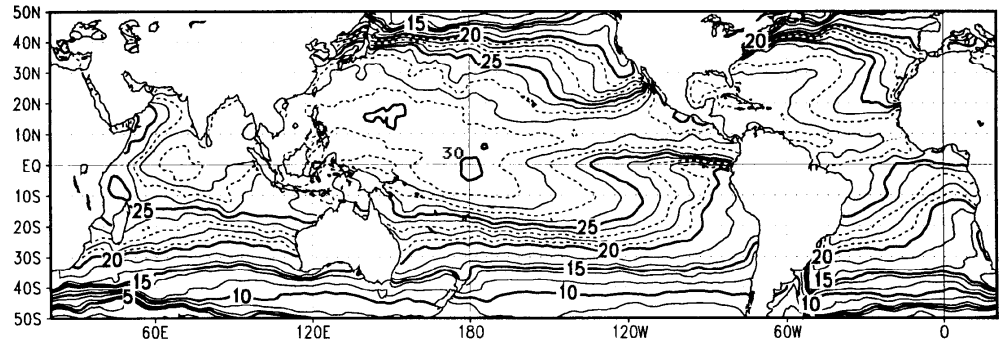

(a)

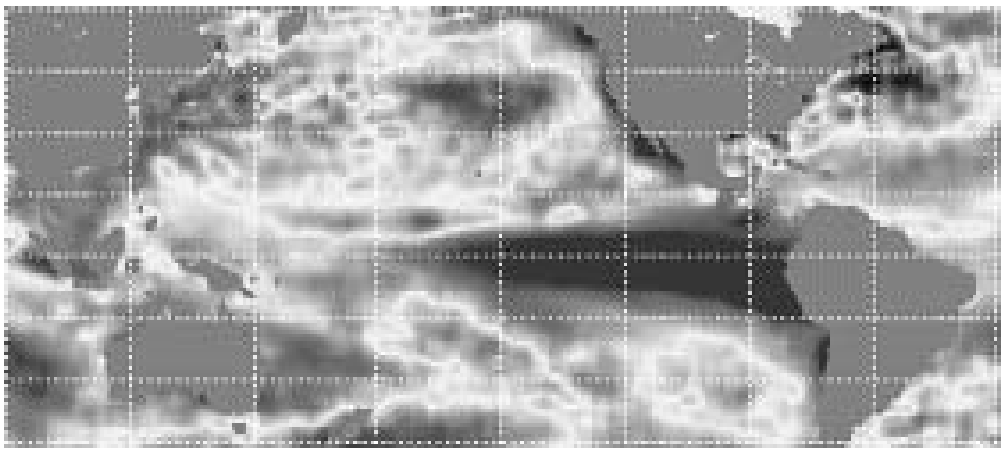

(b)

Figure 1: *Dijkstra and Van der Vaart*

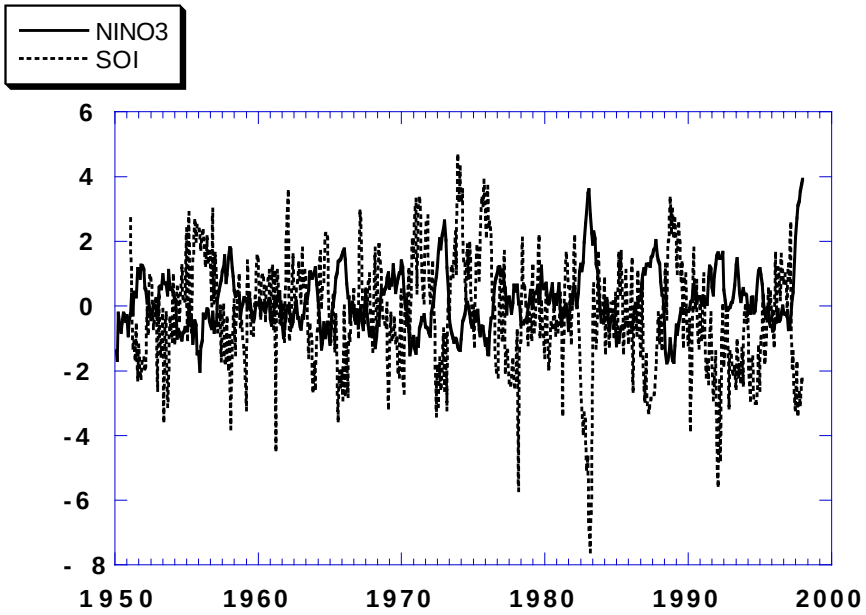

Figure 2: *Dijkstra and Van der Vaart*

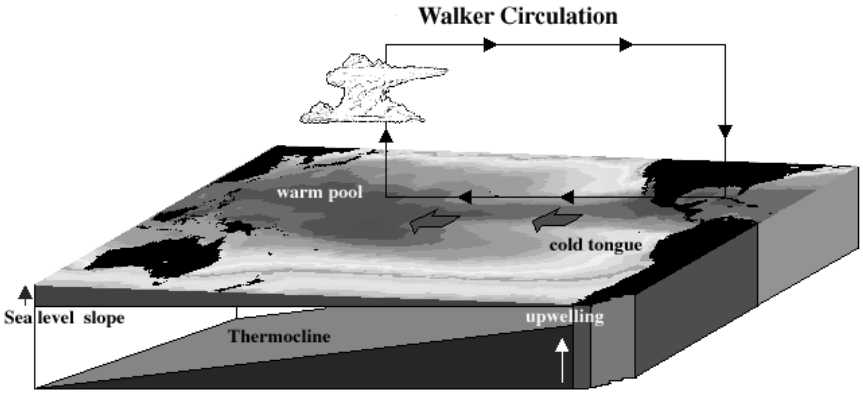

Figure 3: *Dijkstra and Van der Vaart*

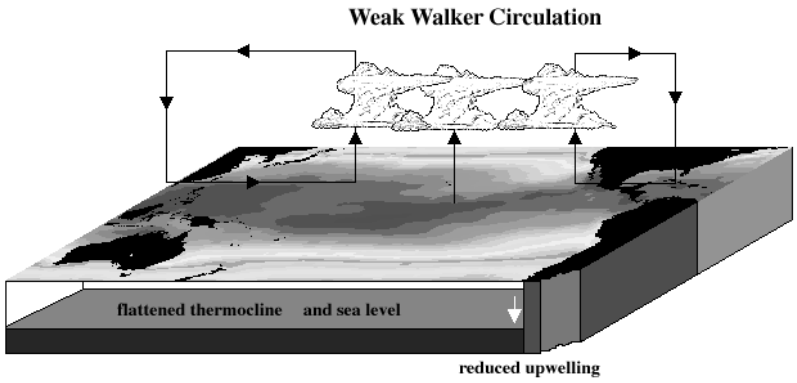

Figure 4: *Dijkstra and Van der Vaart*

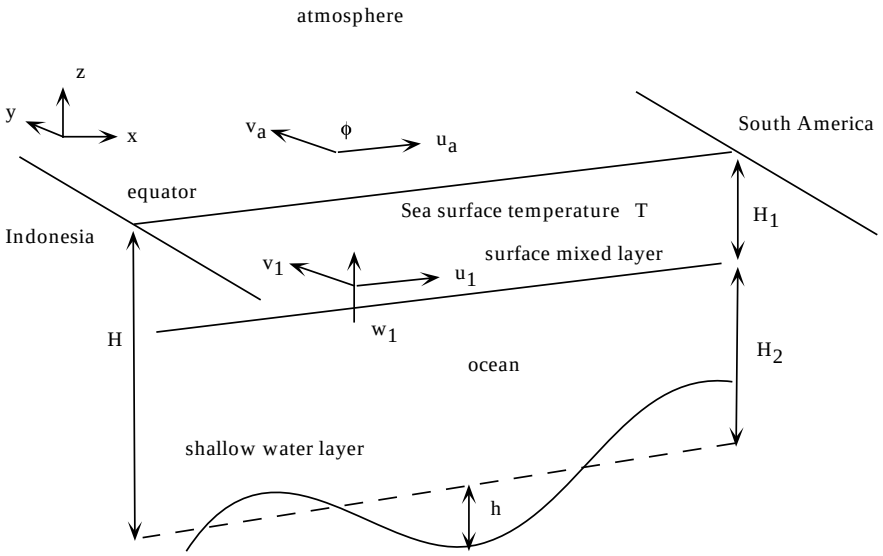

Figure 5: *Dijkstra and Van der Vaart*

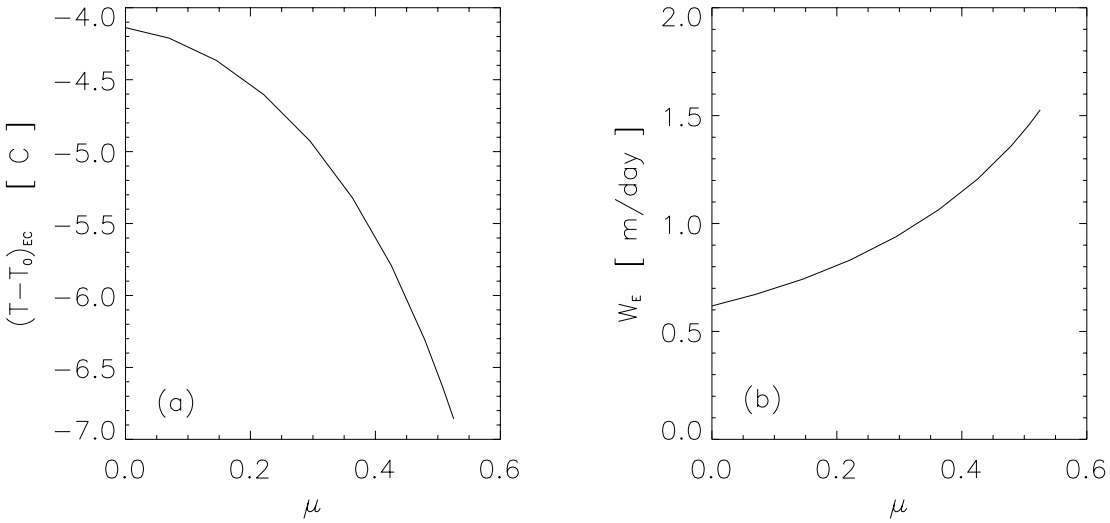

Figure 6: *Dijkstra and Van der Vaart*

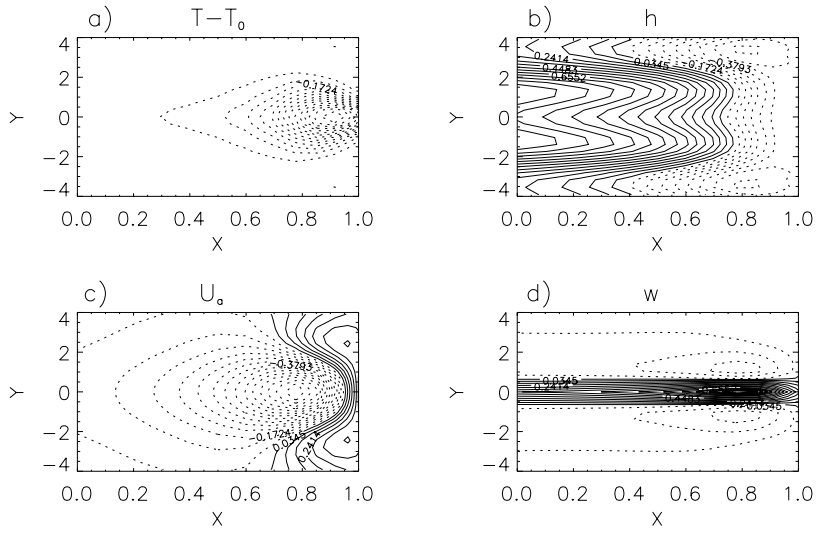

Figure 7: *Dijkstra and Van der Vaart*

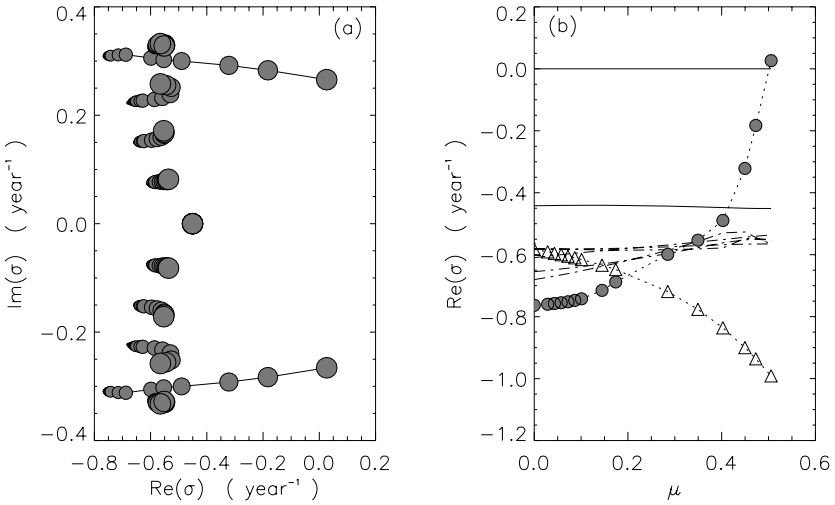

Figure 8: *Dijkstra and Van der Vaart*

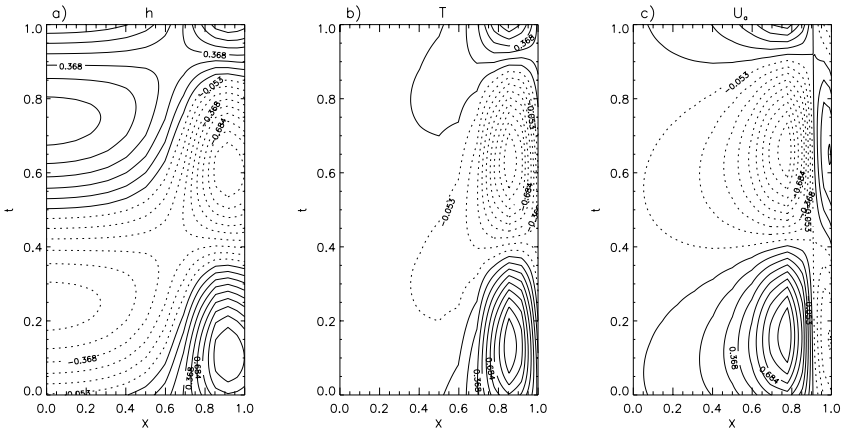

Figure 9: *Dijkstra and Van der Vaart*

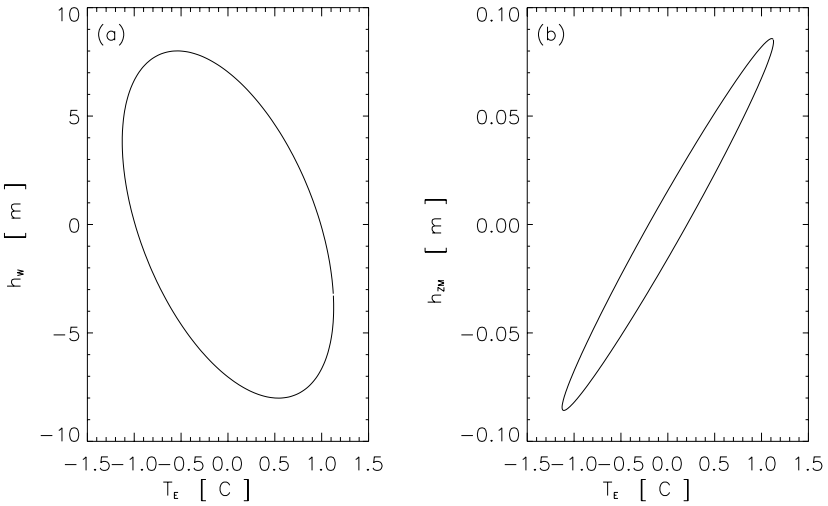

Figure 10: *Dijkstra and Van der Vaart*

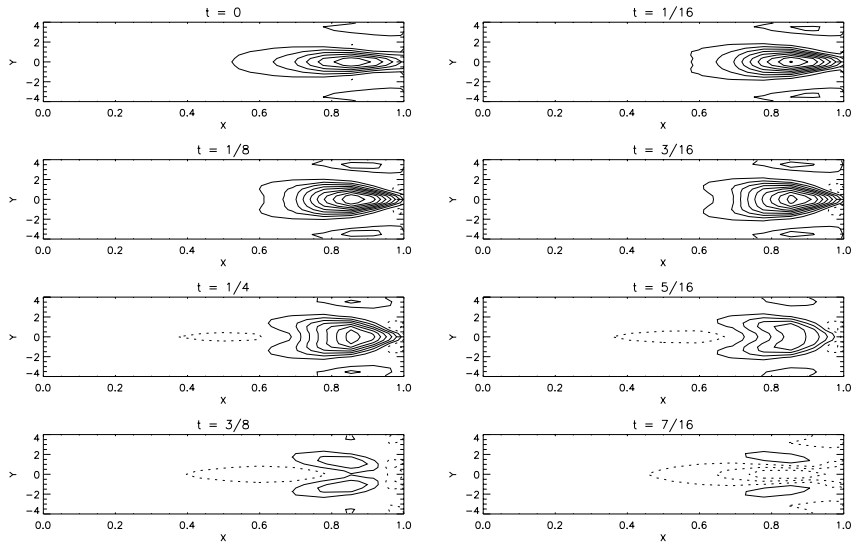

Figure 11: *Dijkstra and Van der Vaart*

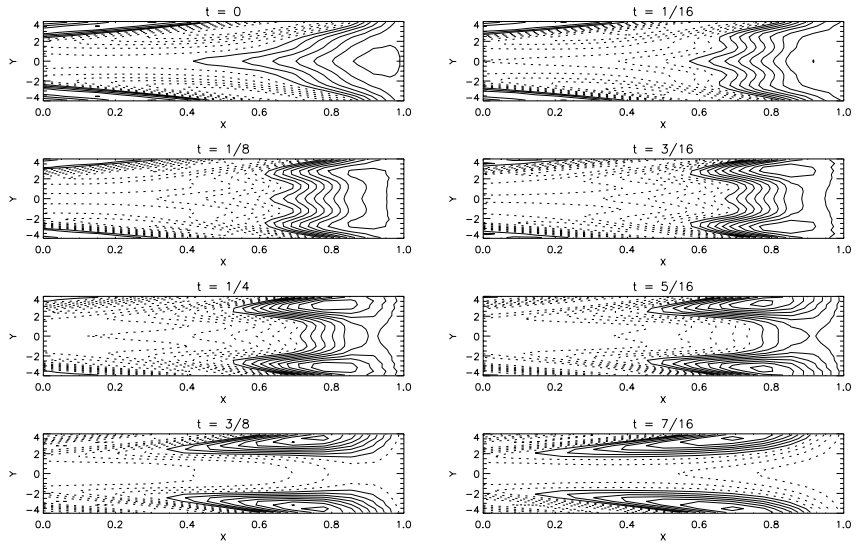

Figure 12: *Dijkstra and Van der Vaart*

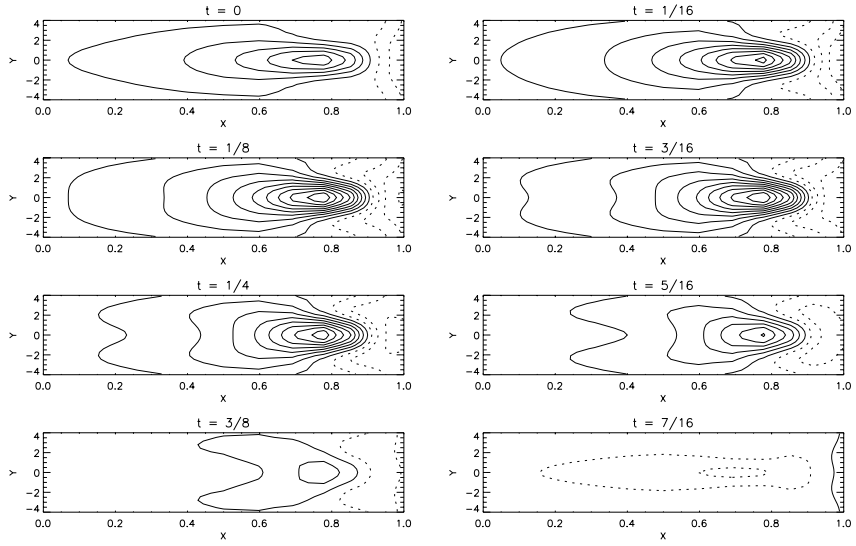

Figure 13: *Dijkstra and Van der Vaart*

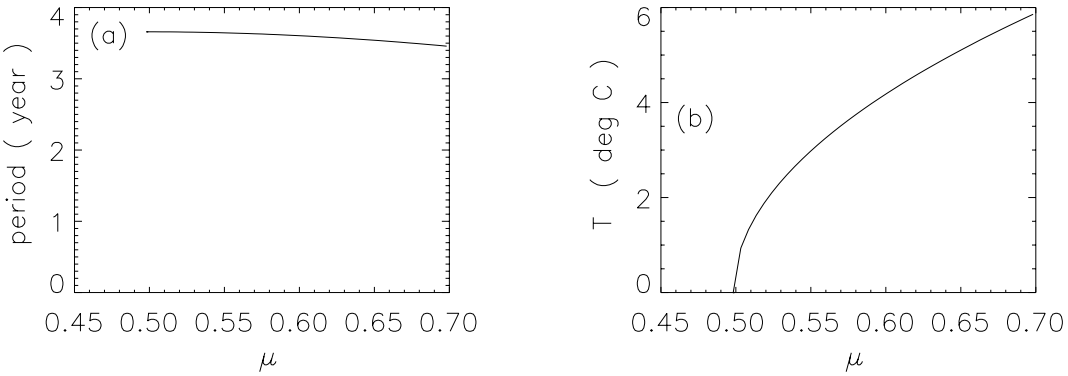

Figure 14: *Dijkstra and Van der Vaart*

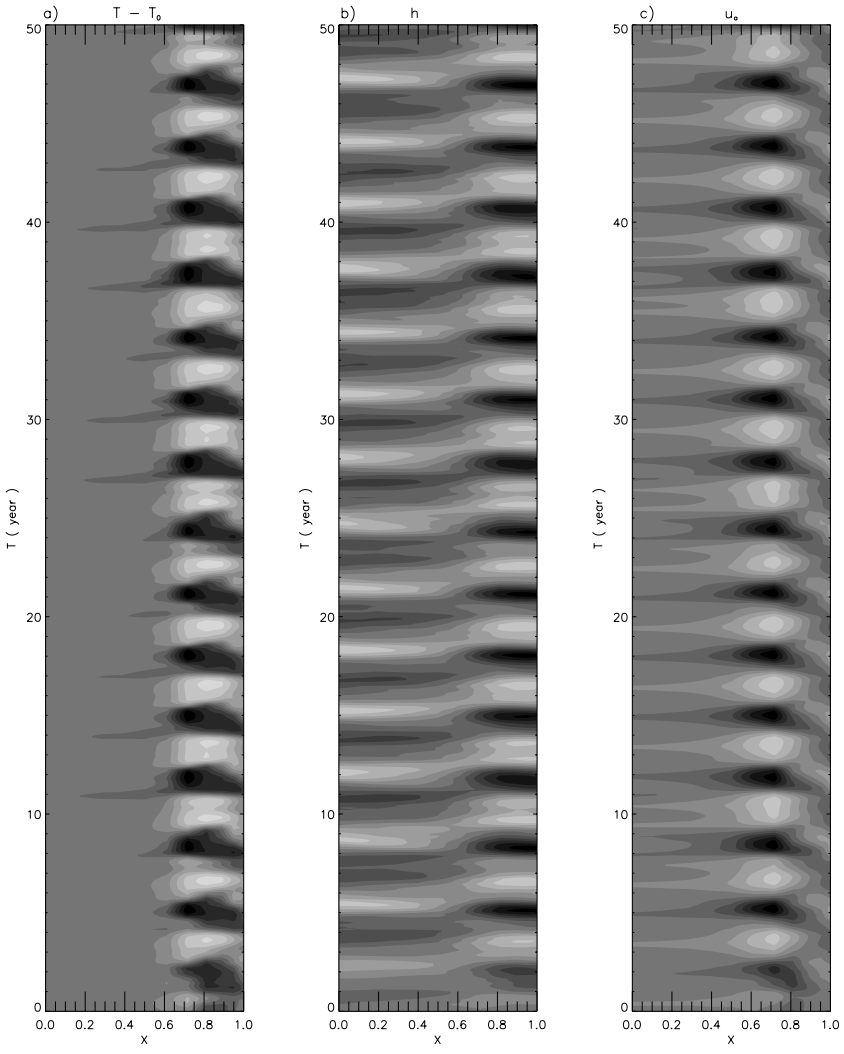

Figure 15: *Dijkstra and Van der Vaart*

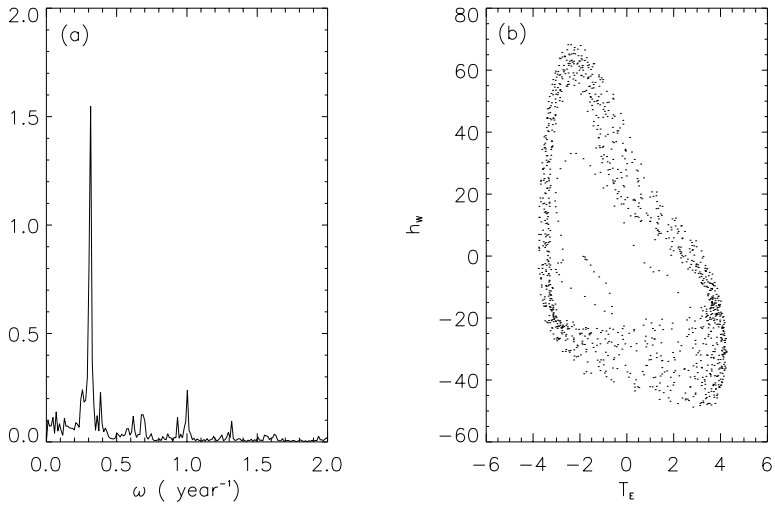

Figure 16: *Dijkstra and Van der Vaart*